Since January 2020 Elsevier has created a COVID-19 resource centre with free information in English and Mandarin on the novel coronavirus COVID-19. The COVID-19 resource centre is hosted on Elsevier Connect, the company's public news and information website.

Electrochimica Acta 404 (2022) 139757

Contents lists available at ScienceDirect

Electrochimica Acta

journal homepage: www.elsevier.com/locate/electacta

PEDOT-AuNPs-based impedimetric immunosensor for the detection of SARS-CoV-2 antibodies

Ana Luiza Lorenzen[a], Ariane Moraes dos Santos[a], Luâni Poll dos Santos[a], Luciano da Silva Pinto[b], Fabricio Rochedo Conceição[b], Franciele Wolfart[a,*]

[a] Instituto Federal de Educação, Ciência e Tecnologia Farroupilha – Campus São Borja, Rua Otaviano Castilho Mendes, 355, Betim, São Borja, RS CEP 97670-000, Brazil

[b] Universidade Federal de Pelotas, Centro de Desenvolvimento Tecnológico, Núcleo de Biotecnologia – Campus Capão do Leão, S/N, Capão do Leão, RS CEP 96160-000, Brazil

ARTICLE INFO

Article history:
Received 21 September 2021
Revised 11 December 2021
Accepted 16 December 2021
Available online 18 December 2021

Keywords:
Impedimetric biosensor
COVID-19
PEDOT
Gold nanoparticles
Impedance spectroscopy
SARS-CoV-2

ABSTRACT

Electrochemical sensors and biosensors are useful techniques for fast, inexpensive, sensitive, and easy detection of innumerous specimen. In face of COVID-19 pandemic, it became evident the necessity of a rapid and accurate diagnostic test, so the impedimetric immunosensor approach can be a good alternative to replace the conventional tests due to the specific antibody-antigen binding interaction and the fast response in comparison to traditional methods. In this work, a modified electrode with electrosynthesized PEDOT and gold nanoparticles followed by the immobilization of truncated nucleoprotein (N aa160–406aa) was used for a fast and reliable detection of antibodies against COVID-19 in human serum sample. The method consists in analyzing the charge-transfer resistance (R_{CT}) variation before and after the modified electrode comes into contact with the positive and negative serum sample for COVID-19, using $[Fe(CN)_6]^{3-/4-}$ as a probe. The results show a linear and selective response for serum samples diluted in a range of 2.5×10^3 to 20×10^3. Also, the electrode material was fully characterized by Raman spectroscopy, transmission electron microscopy and scanning electron microscopy coupled with EDS, indicating that the gold nanoparticles were well distributed around the polymer matrix and the presence of the biological sample was confirmed by EDS analysis. EIS measurements allowed to differentiate the negative and positive samples by the difference in the R_{CT} magnitude, proving that the material developed here has potential properties to be applied in impedimetric immunosensors for the detection of SARS-CoV-2 antibodies in about 30 min.

1. Introduction

Coronaviruses are a family of viruses present in various animal species. There are seven types of coronaviruses capable of infecting humans, three of them cause respiratory disease of different levels of gravity (SARS-CoV, SARS-CoV-2 and MERS-CoV) [1, 2]. SARS-CoV-2 is highly transmissible, and it causes the COVID-19, a disease that already caused more than 4 million deaths worldwide until September/2021 [3]. At the moment, the gold standard for the COVID-19 diagnoses is the reverse transcription polymerase chain reaction (RT-PCR) and the enzyme-linked immunosorbent assay (ELISA), the last one is used to detect specific antibodies in the human blood [1, 4]. Despite the high reliability of these techniques, their high cost, time consumption and the need for trained people and specific equipment configure limitations for their application as large-scale diagnostics tests [1, 4]. In this way, COVID-19 pandemic presents an urgent demand for accurate, low-cost, short-time response, and portable tests, expanding their access for the entire population and helping in the infection control [5–7]. In this context, electrochemical sensors and biosensors respond very well for being fast, inexpensive, sensitive, and easy to perform [8–11]. Moreover, they are robust, easy to miniaturize, require a small analyte volume, and can be applied in human fluids (blood, saliva, urine), food, and environmental samples (air, water, soil) [10].

Electrochemical sensors operate by converting the electric signal into a quantitative or semi-quantitative analytical signal, which can be measured. The signal is derived from some change in the electrode/solution interface, such as an electron transfer reaction or a modification in the electrical resistance, which may be associated with the increased concentration of an analyte of interest [5, 12]. The immobilization of the biomolecular recognition element at the electrode surface characterizes the electrochemical biosensor [5, 12]. This element is chosen according to the specific binding

* Corresponding author.
E-mail address: franciele.wolfart@iffarroupilha.edu.br (F. Wolfart).

https://doi.org/10.1016/j.electacta.2021.139757
0013-4686/

affinity with a target bioanalyte [10, 12], promoting higher sensitivity and lower detection limits, making biosensors especially useful for detecting pathogens-related markers [6, 11]. The main elements used for recognition are antibodies, antigens, enzymes, whole cells and nucleic acids [10, 12]. Electrochemical biosensors offer enough features to accelerate and simplify the bioanalytical process due to the high sensitivity and sensibility, robustness, accuracy, low-cost and mass production capability [13].

The immunochemical reaction of an antigen (AG) binding to a specific antibody (AB) can be explored for the development of biosensors with high recognition capacity [5, 10, 14]. To do so, AG or AB is immobilized on the electrode surface to form a thermodynamically stable AG-AB complex when its pair is present in the analyte [15]. A recent study of the kinetic and thermodynamic interaction between immobilized SARS-CoV-2 nucleoprotein and specific antibodies showed that the immune complex formation has very strict steric requirements features. Also, the estimated Gibbs free energy for AG-AB binding was determined as -34 kJ mol^{-1} [16]. This approach has been applied to design biosensors for diagnosis of infectious diseases, like Dengue [17, 18], Zika [19, 20], Hepatitis [21, 22], Escherichia coli [23, 24] and Middle East Respiratory Syndrome [15]. In the face of COVID-19 pandemic, different immunobiosensors for this disease are found in the literature [6, 25-28]. Mojsoska et al. [6] developed a platform for the detection of the spike subunit 1 protein based on a graphene electrode functionalized with anti-spike antibody. The detection range was determined by the peak current drop of the voltammogram, which decreased with increasing antigen concentration. This immunosensor can be designed on a portable device, providing faster analysis than classic methods, allowing the Point-of-Care diagnosis. A method based on impedimetric immunosensor for the detection of SARS-CoV-2 was developed by Zaccariotto et al. [29], in which, SARS-CoV-2 antibodies were immobilized in the reduced graphene oxide and SARS-CoV-2 spike protein RBD was detected in saliva samples, using $[Fe(CN)_6]^{3-/4-}$ redox couple as a probe.

Different materials have been combined to develop electrochemical biosensors, such as graphene oxide [30], metal organic frameworks [31], conducting polymers [32], gold and silver nanoparticle [33]. Recently, Hashemi et al. [34] related an electrochemical nanosensor based on activated graphene decorated with gold nanostars, capable to detect IgG antibodies against S1 protein of SARS-CoV-2 in human plasma samples. The nanosensor exhibited a good correlation with the ELISA assay, and a very low detection limit (0.18×10^{-19}% V/V) and sensitivity of 2.14 uA (% V/V)$^{-1}$.

In the literature, it is well explored that the high ratio area/volume, manifested by nanoscale materials, favors greater sensitivity due to the signal amplification [35, 36]. Gold nanoparticles (AuNPs) are especially remarkable in the biosensors development, besides their great analytical response, they also have excellent biocompatibility, high conductivity, catalytic activity, and facile surface modification, allowing the easy attachment of desired species on their surface, such as antigens or antibodies [35–37]. However, depending on the conditions, AuNPs tend to aggregate, losing their unique properties mentioned above [38]. Thereupon, it is common their combination with stabilizing agents [39].

Conducting polymers (CP) are interesting materials for the construction of electrochemical sensors because of their electroactivity, electrical conductivity, high surface area, mechanical flexibility, biocompatibility, chemical stability in aqueous solutions, and considerable adsorptive ability [40–42]. The semiconducting properties of conducting polymers have been explored for immunosensor application due to their changes in capacitance and resistance at the electrode / electrolyte interface, that can be monitored by a signal transducer and converted into analytical signal [43].

The modification of the structural and morphological features could be controlled by the polymerization technique. Among different methods to obtain the CP, the electropolymerization has some advantages because it provides stable polymers with high doping level, also allowing the enrichment of the polymer layer with biological or metal compounds present in the synthesis solution, In addition, it is an easy, fast and environmentally friendly method [43]. In general, electrodeposition is widely applied using different electrochemical techniques; the deposition of the material directly on the electrode substrate permits a better adhesion of the film than other techniques like adsorption or coating with previously synthesized polymers. Also, electrochemical deposition allows a better control of the morphology and thickness of the deposited film [44].

The naturally porous structure of the CPs makes them ideal for immobilize nanoparticles and avoid their aggregation, resulting in a nanocomposite material that acquires different properties compared to the isolated materials, usually reflecting on improved conductivity, increased surface area, processability, and mechanical stability [41, 42, 45]. Especially, the high surface area supplied by the CP morphology is a useful feature to improve biosensors performance because it enhances the interfacial contact with the biological element and, consequently, with the sample [40, 42]. Metal nanoparticles can be obtained by wet-chemical methods or electrodeposition, the latter offers some advantages, such as the absence of chemical reductants or oxidants and undesired sub-products, fast synthesis, and the possibility of directly anchoring the nanoparticle to the electrode surface, by an easy and fast method [44, 46]. In addition, the electrosynthesis can be considered an excellent route in order to obtain nanomaterials with exceptional physicochemical properties, such as high electrical conductivity, improved catalytic properties and large surface area, which make them particularly interesting for sensor and biosensor approach [44, 46].

Poly (3,4-ethylenedioxythiophene) or PEDOT, is one of the most widely applied CPs in biologic/biomedicals interfaces due to its superior biocompatibility, in comparison to others [47]. Also, it has characteristic that are required for applications in biosensors, such as stability and high conductivity [38, 41, 47, 48]. The sulfur atoms of thiophene rings in PEDOT structure can establish stable bonds with the AuNPs, due to the strong affinity between them [32, 35, 49]. The combination of these materials can be explored for different application, thanks to the synergism of the CPs high surface area with the electrical conductivity that comes from AuNPs. These features result in higher sensitivity and selectivity, lower detection limits and good reproducibility and stability for sensor and biosensor applications [32, 50]. Furthermore, both materials are biocompatible, establishing an interface for immobilizing the different biological components, such as disease specific antigens, being a useful method to investigate associated biomarkers [32, 38].

Based on that, in this work was developed an impedimetric biosensor for the detection of antibodies against COVID-19 truncated nucleoprotein (N aa160–406aa) antigen. The nucleoprotein was chosen as the target of the assay since it is an immunodominant antigen and is consistently employed to detect antibodies against other coronaviruses in both humans and animals [51, 52] Furthermore, it has high sensitivity and specificity in serological assays and is easily produced in E. coli with low cost [52].

The platform is composed by PEDOT, AuNPs and the antigen, showing to be efficient for antibodies detection in a wide dilution range using human serum samples and being able to differentiate positive and negative serums by the charge-transfer resistance (R_{CT}) magnitude, using $[Fe(CN)_6]^{3-/4-}$ as a probe. This methodology is a good alternative to develop a COVID-19 antibodies test due to the easy processability, selectivity, low cost and rapid detection, with a response time of about 30 min.

2. Experimental section

2.1. Chemical and materials

3,4-Ethylenedioxythiophene (EDOT, 97%), Poly(sodium 4-styrenesulfonate) (PSS), Gold (III) chloride solution ($HAuCl_4$, 99%) and bovine serum albumine (BSA, ≥98%) were purchased from Sigma-Aldrich. Chloride potassium, disodium hydrogen phosphate, potassium phosphate monobasic, potassium hexacyanoferrate (II) trihydrate, potassium hexacyanoferrate (III) were acquired from Neon. Sodium chloride was obtained from Anidrol. All chemicals were used as received. The solutions were prepared using deionized water by Elga Purelab Flex method (18.2 MΩ.cm).

PBS buffer at pH 7.2 was prepared mixing NaCl 137.0 mmol L^{-1}, KCl 2.7 mmol L^{-1}, Na_2HPO_4 10 mmol L^{-1} and KH_2PO_4 2.0 mmol L^{-1}. PBS buffer was used for biological samples dissolution and as electrolyte for electrochemical tests.

All electrochemical procedures were performed in a DropSens μStat-i-400 s and DropView 8400 software. A three-electrodes setup consisting of a steel mesh (geometric area of 0.5 cm^2), platinum wire and $Ag/AgCl/Cl^-_{sat}$ as working, counter and reference electrodes, respectively, was used for all procedures.

2.2. Biological compounds

The recombinant truncated nucleoprotein (rN aa160–406aa) of SARS-CoV-2 was produced in E. coli. Briefly, rN coding sequence was cloned into a pET28-a expression vector (Invitrogen). E. coli BL21(DE3) was transformed with the construct, and expression of the rN was induced with isopropylthio-β-D-galactoside (1 mmol L^{-1} IPTG). Recombinant proteins were purified by Ni-NTA affinity chromatography, quantified using the BCA protein assay kit (Pierce) and conserved in PBS buffer at pH 7.2. The rN reacts with IgG, IgM and IgA antibodies. To appoint the modified electrodes, we called the truncated nucleoprotein (Naa160–406aa) as antigen (AG).

The human serum samples were obtained from hospitalized patients at teaching hospital of Universidade Federal de Pelotas (Rio Grande do Sul – Brazil) with moderate symptoms at 15 to 20 days' post-onset of the symptoms and documented with a positive SARS-CoV-2 RT-PCR test and high antibody reactivity to in-house indirect ELISA immunoassay. The results of the ELISA assay are shown in Table S1 in supplementary material. Negative serum samples were collected prior to the COVID-19 pandemic, the human serum samples were collected in 2018 in the city of Rio Grande (Rio Grande do Sul – Brazil), all samples are non-reactive to in-house indirect ELISA immunoassay.

All biologic samples and the truncated nucleoprotein (N aa160–406aa) were kindly provided by the Federal University of Pelotas, Center for Technological Development, Biotechnology Nucleus at Rio Grande do Sul, Brazil.

Signed informed consent forms were obtained from all patients as per institutional ethical approvals obtained from the Ethics Committee in Federal University of Pelotas and National Commission of Research Ethics (CONEP), reference number 4.043.628.

2.3. PEDOT-AuNPs electrosynthesis and antigen immobilization

The steel mesh electrodes were lightly sanded and cleaned in acetone in an ultrasound bath for ten minutes. After dried, the electrode was modified from solution EDOT 0.01 mol L^{-1} and 7 g mL^{-1} PSS, in pH 5,5 adjusted with hydrochloric acid, by applying a potential of 1.1 V and charge density of 120 mC cm^{-2}. Then, the electrode was washed with deionized water and immersed in 1 mmol L^{-1} $HAuCl_4$ / 0.1 mol L^{-1} KCl solution for ten minutes, followed by a gold reduction step by application −1.0 V until a charge density of 30 mC cm^{-2} was obtained. Next, the PEDOT/AuNPs modified electrode was washed with deionized water and fifteen cyclic voltametric (CV) cycles were performed for film stabilization using PBS buffer pH 7.2 as electrolyte, in a potential range from −0.8 to 0.4 V at scan rate of 20 mV s^{-1}.

For antigen immobilization on PEDOT/AuNPs modified electrode, the electrode was immersed in a solution containing 0.01 µg mL^{-1} truncated nucleoprotein (N aa160–406aa) in PBS buffer for 20 min. After the interaction time, the electrode was washed in PBS buffer pH 7.2 and it was immersed in the 1% BSA solution for 30 min, repeating the buffer washer.

The modified electrodes were named accordingly: PEDOT/AuNPs, PEDOT/AuNPs/AG (after the truncated nucleoprotein immobilization) and PEDOT/AuNPs/AG/BSA (after BSA blocking).

2.4. Serum samples detection

The detection of antibodies in real samples was performed by sequential additions of the serum sample to the electrolyte $[Fe(CN)_6]^{3-/4-}$/PBS in the electrochemical cell, gradually increasing the serum concentration from the dilution factor of 20×10^3 to 2.5×10^3. EIS measurements were recorded after ten minutes of each addition, sufficient time for the AG-AB interaction. The specificity of the biosensor was evaluated by adding the nonspecific serum samples. The average for two different nonspecific serum samples was used as the control for negative test. Both specific and unspecific serum tests were made in triplicate, being prepared new PEDOT/AuNPs/AG/BSA modified electrodes for each replicate, since specific antigen-antibody binding and also unspecific adsorptions on the electrode surface do not allow to reuse the electrodes.

2.5. Characterization

All the electrochemical characterizations were done in 1 mmol L^{-1} $[Fe(CN)_6]^{3-/4-}$ electrolyte in PBS buffer pH 7.2. Firstly, the modified electrodes were characterized by cyclic voltammetry in a potential range of −0.5 to +0.7 V at a scan rate of 20 mV s^{-1}. Each EIS measurements was recorded applying the peak oxidation potential (Fe^{II}/Fe^{III}) previously obtained by the voltammogram (all the oxidation peaks were around 0.3 V). The frequency ranged between 10 kHz-10 mHz and the perturbation amplitude of 10 mV was maintained constant. The morphologies of modified electrodes were investigated by Scanning Electron Microscopic (SEM) in a TESCAN VEGA3 LMU coupled with the energy dispersive spectroscopy (EDS) detector and Transmission Electron Microscopic (TEM) in a JEOL JEM 2100. All SEM and TEM images were recorded directly on steel mesh modified electrodes and the images presented herein are the representative ones, since at least five different points were checked to assure the homogeneity of the modified electrodes, and approximately 100 nanoparticles were counted and measured for size distribution using the ImageJ software. Raman spectra were recorded in a spectrometer Bruker Senterra II, with excitation laser 532 nm and potency of 0.2 mW, with 3–5 cm^{-1} resolution.

3. Results and discussion

Chemically modified electrodes are commonly investigated using redox probes, such as potassium ferro / ferricyanide ($[Fe(CN)_6]^{3-/4-}$), since the electron transfer charge depends on the electrode interface characteristics, mainly its chemical nature [53]. Thus, the modification steps can be observed by the electrochemical measurements performed on $[Fe(CN)_6]^{3-/4-}$ / PBS electrolyte. Fig. 1(a) shows the voltammograms of the modified electrodes in $[Fe(CN)_6]^{3-/4-}$ / PBS electrolyte, in which two redox behaviors are observed. The first one, located around −0.5 V / −0,.2 V, is related to PEDOT redox reaction, as detailed by Sterby et al. [54].

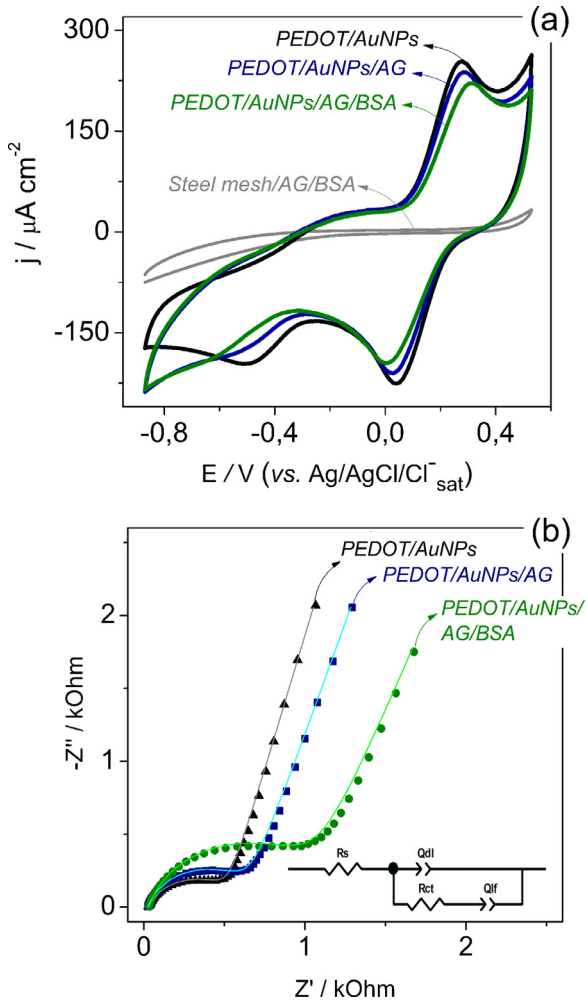

Fig. 1. (a) Cyclic voltammograms recorded at $v = 20$ mV s^{-1} and (b) Nyquist plot. All measurements were performed in 1.0 mmol L^{-1} $K_4Fe(CN)_6$/ $K_3Fe(CN)_6$ in PBS buffer pH 7.2 for the PEDOT/AuNPs modified electrodes (black line), after antigen immobilization (blue line), BSA blocking (green line) and steel mesh/AG/BSA (gray lines in (a)). The solid lines in the Nyquist plots represent the experimental data fitting using the equivalent circuit inserted in the figure.

Another redox process is located at 0.3 V / 0.0 V, that is associated with $Fe(CN)_6^{4-/3-}$ conversion by electron transfer and its well-defined peak profile suggests that the process occurs by diffusion [53]. A shift towards higher potential values and a decrease in peak current intensity are observed in the voltammograms after AG and BSA immobilization, suggesting an increasing difficulty for the $Fe(CN)_6^{4-/3-}$ redox reaction to occur at the electrode / electrolyte interface. The protein layer act as a barrier preventing the $Fe(CN)_6^{4-/3-}$ ions to approach the electrode surface, so the shift in redox peaks and the decrease of current density can be attributed to the insulating character of the biological components on the electrode surface, as well as the proteins steric hindrance effect [55, 56]. The diminishment of PEDOT cathodic peak can be attributed to the steric effect caused by the biological compounds attached at the nanocomposite, which makes the ions approximation at electrode/electrolyte interface more difficult and hampers the ions insertion / expulsion from polymeric matrix during PEDOT redox process, since the biomolecules can partially block the modified electrode active sites after the immobilization [57]. In addition, no redox behavior was observed for the unmodified electrode (steel mesh/AG/BSA) in the investigated potential range, as shown in Fig. 1(a).

To further investigate the electrochemical interfacial process of the modified electrodes, EIS experiments were carried out and the Nyquist plots are shown in Fig. 1(b). The analysis of EIS data from conducting polymers and nanocomposites could be subject of different interpretation, so the choice of the correct equivalent circuit model that represents the electrical effects of the electrochemical systems, as well as describes the mechanism of the reaction, needs a careful understating of the individual physical properties of each system [58, 59]. After a careful consideration of the different approaches reported elsewhere [58–61] to interpret the EIS results of conducting polymers, also considering the factors governing the electrochemical impedance on protein-modified surface, the results presented here were fitted using an equivalent circuit model composed by a combination of resistors and capacitors.

Nyquist plot in Fig. 1(b) shows a classic conducting polymer profile, wherein the semicircular segment is related to the charge-transfer resistance and the double-layer capacitance, and the linear segment is associated with the ions intercalation in the polymeric film to maintain the charge neutrality during the redox processes [17, 62, 63]. It is clearly seen in Fig. 1(b) the increase of the semicircle at the high frequency region according to the biomolecules incorporation in the nanocomposite film (PEDOT/AuNPs). In order to evaluate this effect, EIS data were fitted using the equivalent circuit model inserted in the Fig. 1(b). This equivalent circuit is composed by a series resistance contribution (R_s), that accounts for electrolyte and current collector resistance, a charge-transfer resistance (R_{CT}), related to the interfacial Faradaic process, a constant phase element (Q_{dl}), representing the double-layer capacitance, and another constant phase element (Q_{lf}), related to the low-frequency capacitance that accounts the intercalation processes in the polymeric matrix [63, 64]. Lastly, n parameter accounting the non-ideality factor related to the constant phase element is present, where the n value ranges from 0 to 1, being 1 the value representing the constant phase element as an ideal capacitor. The calculated values are summarized in Table 1.

The increases in the R_s can be related to intrinsic resistances of the electronic transport at the polymeric film since the electrolyte and current collector were all the same for the different measurements. Both Q_{dl} and Q_{lf} values decreased as the antigen and BSA were attached at the electrode surface; these diminishments can be associated with changes in the film morphology. This proposition is supported by SEM images (Fig. 3), since Q_{dl} is related to the electrode / electrolyte interface area, and the decrease of the Q_{lf} values can be attributed to the blocking effect of the polymeric active sites by the biomolecules. These results corroborate the behavior observed in the cyclic voltammograms. R_{CT} values increment indicates the increase in charge-transfer resistance at the electrode / electrolyte interface after the biomolecules incorporation at the electrode, as will be better discussed below.

PEDOT/AuNPs composite material is intrinsically conductive, easily exchanging electrons with the ions probe. In biosensor application, the electrochemical response in the presence of $Fe(CN)_6^{4-/3-}$ could be influenced by two effects: ionic attraction / repulsion and steric hindrance [55, 65]. The biological species incorporation at the interface hinders the approximation of the ions probe, due to the steric hindrance; in parallel, it enhances their electrical resistance due to the non-electroactive nature. The conductivity changes in the electrode interface can be detected by EIS measurements, specifically analyzing the R_{CT} parameter [65]. In this work, R_{CT} was used to study the system response during the modification step and, later, for the antibody detection. This parameter is directly related to the electronic transference kinetics of the $[Fe(CN)_6]^{3-/4-}$ ions at the electrode / electrolyte interface, being sensitive enough to detect variations in this interface related to the presence of non-electroactive species. An increase in the semicircle diameter is associated with a higher R_{CT}. Fig. 1(b) and fit-

Table 1
Parameters values calculated from the EIS data fitting.

Modified electrode	R_s / kOhm	R_{CT} / kOhm	Q_{dl} /10^{-5} F s^{n-1}	n_{dl}	Q_{lf} /10^{-3} F s^{n-1}	n_{lf}
PEDOT/AuNPs	27.61	548.10	7.11	0.75	0.94	0.84
PEDOT/AuNPs/AG	28.11	678.00	5.43	0.80	0.92	0.80
PEDOT/AuNPs/AG/BSA	30.40	1105.00	5.02	0.82	0.87	0.77

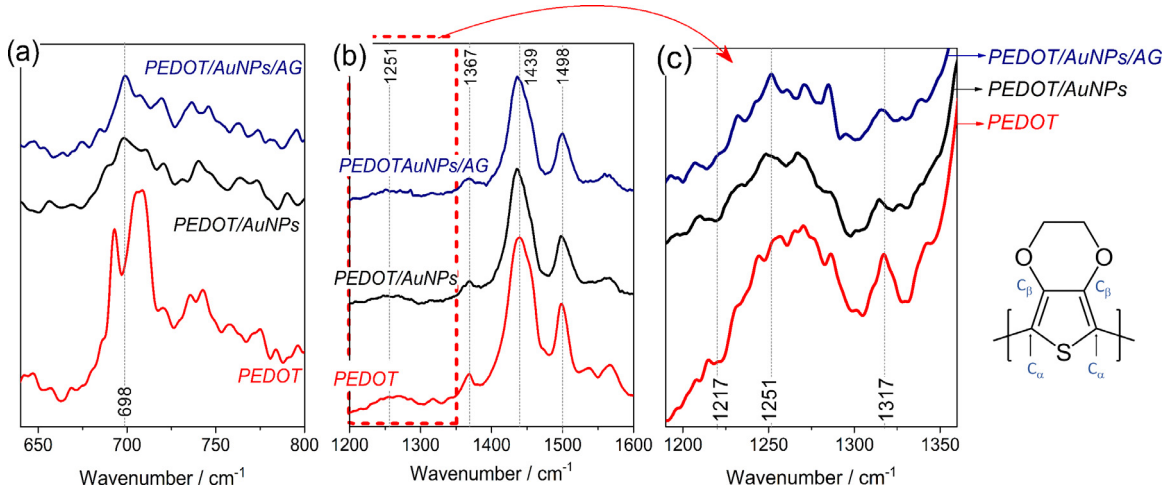

Fig. 2. Raman spectra obtained for PEDOT, PEDOT/AuNPs and, PEDOT/AuNP's/AG. (a) emphasis in the region around 698 cm^{-1} highlighting the AuNPs effect on the pristine PEDOT vibrations; (b) range from 1200 – 1600 cm^{-1} showing the main bands of each material; and (c) the range from 1190 cm^{-1} to 1360 cm^{-1}, highlighting the antigen influence on the material electrode (c). Radiation incident λ = 514 nm. PEDOT monomeric structure is inserted in the figure. The full spectra are show in the Figure S2 in supplementary material.

ted parameters (Table 1) clearly show that R_{CT} increases with both antigen and BSA immobilization on PEDOT/AuNPs electrodes, reflecting the higher difficulty of charge transfer process to occur in the presence of the insulating biological layer on the electrode.

In addition, EIS measurements were carried out for unmodified electrodes. The Nyquist plot and fitting parameters are shown in the Figure S1 and Table S2, respectively, in the supplementary material. The increases observed in the R_{CT} values can be attributed to electrostatic interactions between protein charges and the characteristic charge of the steel mesh. According to Omanovic and Roscoe [66] the protein adsorption occurs when any protein-containing fluid comes into contact with a foreign surface. Although the interaction between metal surfaces and biological compounds is a complex matter, this phenomenon can be related to electrostatic interactions between protein charges and the characteristic charge of the metal [66]. However, as will be discussed later in the serum samples detection, the unmodified electrode do not have ability to differentiate positive and negative serum samples for COVID-19.

In order to show that the nanocomposite was successfully electrosynthesized, Raman spectra were recorded, and the results are shown in Fig. 2. The pristine PEDOT spectrum attributions are compiled in Table S3 in supplementary material, as previously described elsewhere [67–73]. In our analysis, some bands stand out as the signals at 495 and 995 cm^{-1} associated to oxyethylene ring deformation, the band at 692 cm^{-1} assigned to symmetric deformation of C_α-S-C_α, in 1131 cm^{-1} related to C–O-C bond and the weak band at 1252 cm^{-1} attributed to C_α-C_α inter rings [67, 70, 71]. The signals centered at 1367, 1439, and 1500 cm^{-1} are attributed to C–C, C = C(-O) e C = C stretching, respectively [67, 68, 70].

Raman resonant effect occurs in conducting polymers by the incidence of radiation at wavelengths that coincide with the allowed electronic transition band, resulting in a considerable increase in the intensity of the spectrum bands [73]. By this, PEDOT signals are dominant in the Raman spectra and the influence of other constituent materials normally can be detected by possible changes in the profile and position of the PEDOT bands. Therefore, AuNPs incorporation in the polymeric matrix is evidenced by a band shift from 692 to 698 cm^{-1}, accompanied with the significant intensity decrease in this signal (Fig. 2(b)), which can be a result from the interaction between the gold nanoparticles and the sulfur atom present in the PEDOT thiophene ring and this behavior is well recognized in the literature [68, 74, 75]. The deconvolution of the spectra is shown in the supplementary material (Figure S3 (a-c)), where the changes are better observed. The decrease in signal intensity at 439 cm^{-1}, 526 cm^{-1} and 1252 cm^{-1} also confirms this interaction and is related to the thiophene ring deformation [75].

The AuNPs effect on the vibrational modes of PEDOT also can be observed by slight changes in the other bands, such as the decrease in intensity of the signal at 1500 cm^{-1} and the slight band displacement at 1439 cm^{-1}. The latter is attributed to the C = C(-O) stretching, and it can reflect a change in PEDOT oxidation levels when a widening and loss of band intensity is observed [70].

Raman spectrum after antigen immobilization was also recorded, showing a strong evidence of antigen immobilization on the PEDOT/AuNPs modified electrode by a change in the intensity of the band around 698 cm^{-1}, which increases by the interaction between biological compound and the gold nanoparticles through carbon-sulfur bonds, indicating that covalent grafting was successfully done (Fig. 2(c) and S3) [74, 76]. However, others weak signals referring to the secondary structure of the protein are difficult to see due to the high intensity polymeric bands. The main differences in the vibration fingerprint before and after the antigen immobilization step are concentrated in the spectrum range between 1200 cm^{-1} to 1360 cm^{-1} highlighted in Fig. 2(c). As reported elsewhere [76, 77], this region gathers the amide III vibration modes, which range from 1198 to 1224 cm^{-1}, 1251–1267 cm^{-1} and 1318 to 1346 cm^{-1}, and it can be extended up to 1680 cm^{-1} to include amides I analysis [77]. However, in our case, possible

Table 2
Raman signals for the modified electrodes.

	Wavenumber / cm^{-1}			
Modified electrode	C-S-C deformation	Amide III	C –C stretching for PEDOT and Amide III for antigen	Amide III (α-helix)
PEDOT	692	–	1251	–
PEDOT/AuNPs	698	–	1248	–
PEDOT/AuNPs /AG	699	1217	1251	1315
Literature [69, 74, 76, 77]	691–698	1208 / 1224	1250 (for PEDOT) 1240–1250 (Amide III)	1320

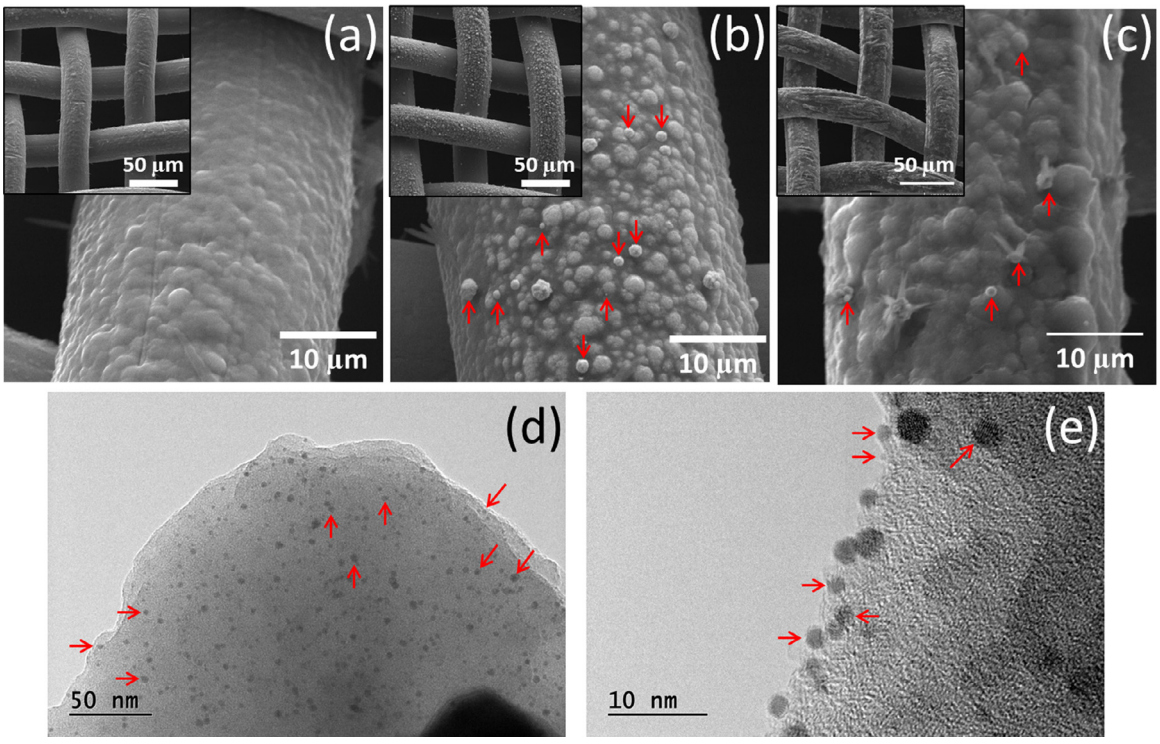

Fig. 3. Representative SEM images of (a) PEDOT (b) PEDOT/AuNPs and (c) PEDOT/AuNPs/AG modified electrodes in an increase of 800 and 3500 times, with voltage acceleration of 20 kV. (d-e) Representative TEM images of PEDOT/AuNPs/AG modified electrodes in different magnitude. Some AuNPs is marked with red arrows in the figure.

differences registered in the higher wavenumber range are masked by the PEDOT vibrational modes. For this reason, the spectra in Fig. 2(c) were deconvoluted making a weak signal at 1217 cm^{-1} visible only for PEDOT/AuNPs/AG modified electrode, indicating the amide groups contribution (Figure S3 in supplementary material) [69, 76, 77]. Moreover, the signal at 1251 cm^{-1}, attributed to PEDOT carbon atoms stretching, slightly changed with the modification steps, becoming well-defined after antigen immobilization, since amide III vibration modes contribute to this spectrum region. The amide III α-helix conformation is expected at 1315 cm^{-1} and is observed in Fig. 2(c), by the shift of Raman band profile. Although PEDOT and PEDOT/AuNPs electrodes also record signals in this region, the bands attributions have not been clearly determined. The main differences registered in the spectra of each electrode modification step are gathered in Table 2. Raman studies are in accordance with the electrochemical results, indicating that the antigen and BSA were successfully immobilized at PEDOT/AuNPs modified electrodes.

The SEM images were obtained from PEDOT; PEDOT/AuNPs and PEDOT/AuNPs/AG modified electrodes in order to investigate the morphology of the materials. From images shown in Fig. 3(a-c) it is possible to see changes in the modified electrodes morphology; the electrosynthesis of PEDOT forms a thin homogeneous film covering the entire steel mesh electrode surface as shown in the Fig. 3(a), with a globular morphology typical of electrosynthesized conducting polymers [78, 79]. For PEDOT/AuNPs modified electrode, it can be seen in Fig. 3(b) the occurrence of small particles with spherical shape and varying sizes, distributed throughout the polymeric film, suggesting the successful electrodeposition of gold. AuNPs are identified by the clearest contrast due to their greater electronic density, allowing them to be distinguished from PEDOT. In Fig. 3(c), the antigen immobilization can be observed by the lower contrast region, suggesting the presence of the biological molecules on the modified electrode, in addition, a greater surface roughness is observed, suggesting that the antigen was uniformly distributed on the PEDOT/AuNPs surface, corroborating the Raman and electrochemical studies.

A better observation of the AuNPs was obtained by TEM representative images shown in the Fig. 3 (d-e). The observed spherical and darker spots are attributed to the gold nanoparticles which are homogeneously distributed over the sample and are involved by the organic materials, represented by the lighter region. The nanometric size ranging from 2 to 16 nm with an average value of 5 nm, but 85% fall in the range of 2 to 8 nm, as shown in Figure S5 in the supplementary material. Also, nanoparticle aggregations were not observed, which is an important characteristic for biosensors application, allowing to explore the entire interfacial region provided by the nanoscale and maximizing the gold-antigen interaction. TEM and SEM techniques also reinforce one of the advantages of combining the conductive polymer with metallic nanoparticles, which is the contribution to nanoparticle stabilization.

Table 3
Semi-quantitative elemental composition of the electrode materials by EDS analysis.

	Elemental composition (%)		
Element	PEDOT modified electrode	PEDOT/AuNPs modified electrode	PEDOT/AuNPs/AG modified electrode
S	5.04	6.70	3.95
Au	–	27.62	22.71
N	–	–	0.96

Note: The complete table is available in Table S4 in the supplementary material.

A further investigation of SEM images was made by Energy Dispersive Spectroscopy (EDS) analysis, which provides an elemental composition of the observed areas, by this, several spots in different SEM images were chosen for PEDOT, PEDOT/AuNPs and PEDOT/AuNPs/AG electrodes (Figure S4 in supplementary material). The results related to one representative spot for each electrode are shown in Table 3. EDS analysis suggests the gold element occurrence in high quantity in the lighter regions of PEDOT/AuNPs electrode images. The presence of the nitrogen element was observed only for PEDOT/AuNPs/AG electrode, indicating the presence of the amino acid groups that compose the antigens protein structure. These results are in agreement with Raman and EIS studies, suggesting that the electrode was successfully modified with the antigen. Other elements identified by the EDS analysis are related to steel mesh composition and to PBS buffer solution, and are fully listed in Table S4, in the supplementary material.

The antibody detection in real samples was analyzed by the impedimetric response of the PEDOT/AuNPs/AG/BSA electrodes against positive and negative serum samples for COVID-19. All the detection tests were performed at a controlled temperature of 23 °C and $[Fe(CN)6]^{3-/4-}$ in PBS buffer pH 7.2 as electrolyte. Buffer systems are widely used for biological research due to their ability to chemically stabilize proteins, preserving their activity, and because the pair of $H_2PO_4^-/HPO_4^{-2}$ helps to maintain a constant pH around 7.0, which is the physiological pH [80]. Due to the adsorption process, each electrode was used only once, therefore, the ΔR_{CT} is based on the EIS measurements of the PEDOT/AuNPs/AG/BSA electrode before contact with the serum sample.

Nyquist plot in Fig. 4(a) shows a larger semicircle diameter for the electrode exposed to positive serum sample due to the highly specific AG-AB interaction, recording the ΔR_{CT} value of 2.80 kOhm. An increase in resistivity to the negative test is also observed (ΔR_{CT} = 1.56 kOhm), but of much lower intensity due to unspecific interactions of the other sample components with the electrode interface [16]. The small increment in the impedance response of negative serum samples can be attributed to the non-specific adsorption of species present in the complex serum matrix [81–84]. This non-specific reaction can occur due to a variety of reasons, for instance, protein-protein interactions, surface proteins denaturation, substrate stickiness, non-specific electrostatic binding to charged surface, and adsorption of molecules in free spaces at the electrode surface [83]. These phenomenona can lead to an increment in the R_{CT} values, as observed for negative sample. However, the increase of R_{CT} values obtained for positive samples is greater, suggesting that the material has good properties to identify the presence of SARS-CoV-2 antibody in real samples. The same conclusion has been reported for modified screen-printed gold electrodes for the diagnosis of caninse visceral leishmaniasis [84], screen-printed electrode based on carbon nanotube-polypyrrole composite to detection of Zika virus in serum sample [85], and electrochemical paper-based analytical device modified by spike protein immobilized on graphene oxide to detect SARS-CoV-2 antibody [86]. Furthermore, the cross-reactivity of the recombinant antigen used in the immunosensor was evaluated

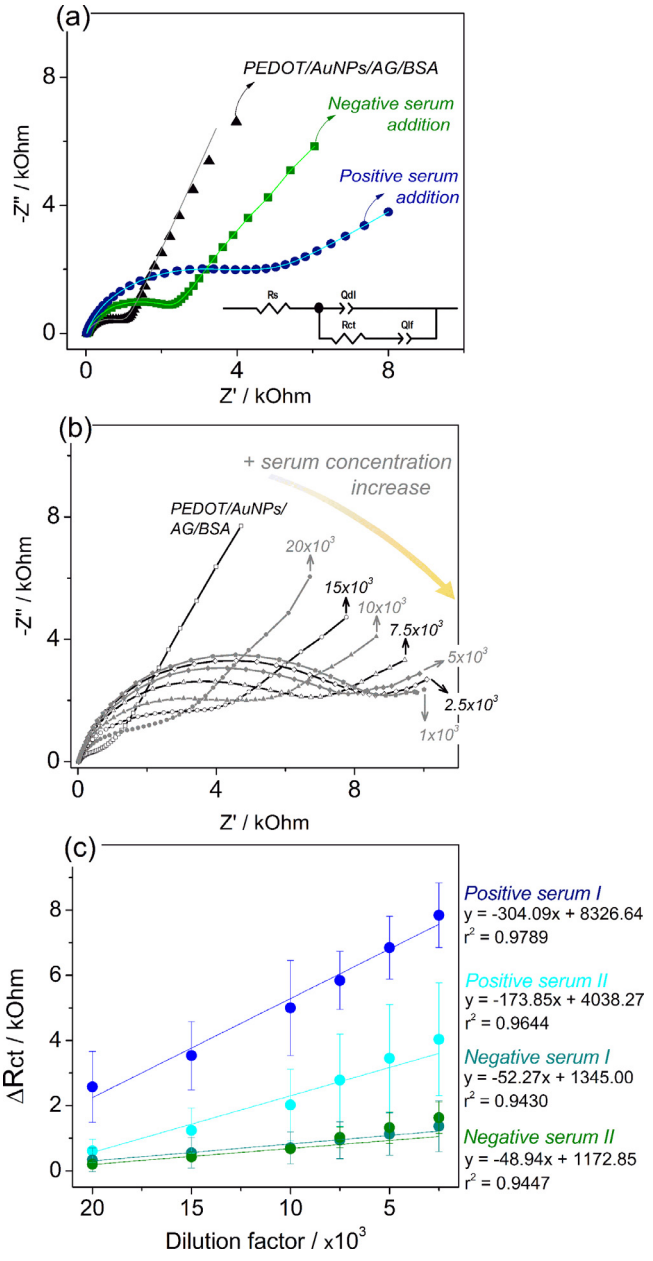

Fig. 4. (a) Comparative Nyquist plot for positive and negative serum samples for COVID-19 in 2.5 × 10^3 dilution factor. The solid lines represent the simulation of the experimental data according to the proposed equivalent circuit, inserted in the graph. (b) Nyquist plot of the PEDOT/AuNPs/AG/BSA modified electrode to different positive serum concentrations. (c) Analytical curves for the evaluated serum samples (n = 3). The solid line represents the linear fit and the respective linear regression is present. The error bars show the standard deviations of three measurements.

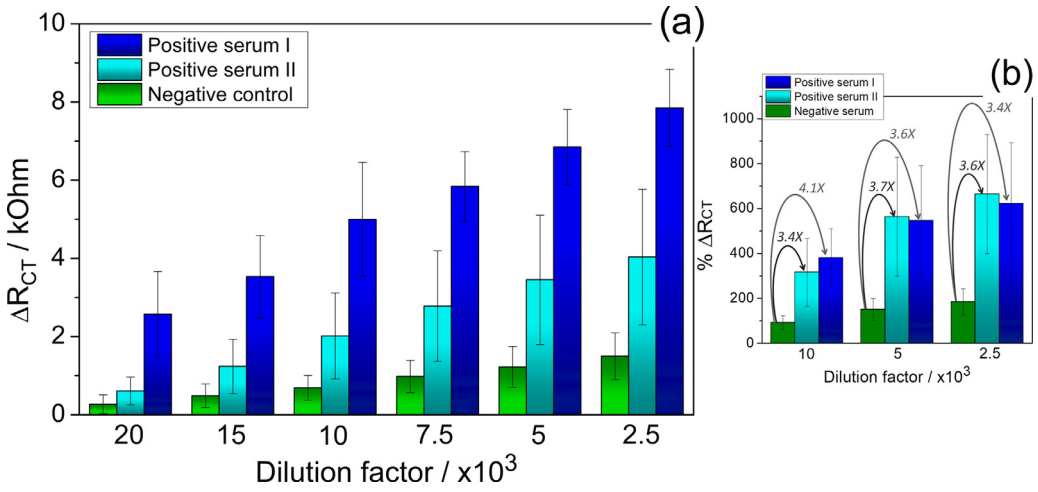

Fig. 5. (a) R_{CT} values for positive and negative serum samples for COVID-19 in different dilution factors ($n = 3$). (b) Comparison of R_{CT} increase rate at some dilution factors for the positive serum samples and negative control serum. The values indicate the ratio of increase in R_{CT} percent response rate. The error bars show the standard deviations of three measurements.

in indirect ELISA with pre-pandemic sera positive for HIV, toxocariasis, dengue, Zika, yellow fever, measles, influenza, hepatitis B and D or parvovirus (unpublished data), which proved to be irrelevant (95% specificity). The cross-reactivity test using the PEDOT/Au/NPs/AG/BSA modified electrode will be present in a future work.

The analytical performance of the PEDOT/AuNPs/AG/BSA electrodes was evaluated by adding successive aliquots of the serum in the electrolyte, gradually increasing its concentration within a range of dilution factor from 20×10^3 to 2.5×10^3 and the R_{CT} value was determined by the mathematical fitting of the EIS curves, applying the same electrical circuit discussed above in Fig. 1(b), and inserted in Fig. 4(a). The enlargement of semicircle diameter in the Nyquist plot (Fig. 4(b)) indicates the increased charge-transfer resistance with each serum addition, which results from specific interaction between antibodies present in the sample with the antigen immobilized at the electrode surface. This specific AB-AG-interaction affects the impedance response because of the increased steric hindrance at the electrode / electrolyte interface. Also, the R_{CT} value could be increased due to the presence of non-eletrocative species on the electrode surface, as previously discussed [65].

In addition, the impedimetric sensor displays a linear response within the evaluated dilution range, as represented in Fig. 4(c), showing a greater slope module inclination for the positive serum samples than negative serum samples. These results reflect the specific AG-AB interaction occurrence in the positive serum samples. The registered curves slope for negative samples are similar to each other, while there is a difference in the curve slopes for the positive serums. This observation can be associated with different antibody levels present in the patient's body at the sample collection moment [81, 87], indicating the potential for this sensor to perform quantitative measurements of antibodies in the samples. This characteristic could not be exploited at this time. The samples nature explains the magnitude of the standard deviation values, since the serum is a complex matrix, containing a variety of other antibodies and proteins that can nonspecifically interact with the electrode interface, resulting in a wider distribution of R_{CT} values for the replicates of the assays [81, 82].

Fig. 5(a) gathers the impedimetric sensor responses against the positive and negative serum samples for COVID-19, at different diluted samples. The assays with specific antibodies samples showed a more expressive average R_{CT} increment compared to the negative control, for all tested dilutions, as verified by the bars profile in Fig. 5(a) and by the percentage values highlighted in Fig. 5(b). The positive serum samples showed more than 3.5-fold the average % ΔR_{CT} increment over negative samples for the tested dilution range (Fig. 5(b)). Also, it is important to be noted that the ΔR_{CT} value for negative serum sample do not increases by increasing the concentration as it does for the positive serum sample, suggesting a good selectivity of the electrode (Fig. 5(a)), as discussed above. Furthermore, the ΔR_{CT} results are in agreement with the ELISA test (Table S1, in supplementary material). Due to the higher affinity, IgG and IgA class antibodies probably dominate the immunosensor reaction, so the reactivity of positive serum I was greater than that of positive serum II. In the ELISA, the IgA and probably IgG levels of positive serum I are higher than those of positive serum II. The fact that positive serum II has a higher IgM level than positive serum I suggests that the IgG level of positive serum I is higher than that of positive serum II. In addition, it is relevant to highlight that the time necessary to AG-AB interaction was fixed in 10 min and the complete EIS measurement took about 20 min, so the results were obtained in approximately 30 min, which is a shorter time when compared to the ELISA assay.

Similar tests for unmodified electrodes (steel mesh/AG/BSA) for negative and positive serum samples at dilution factor of 10×10^3 were carried out and the results are shown in the Figure S1(b) in the supplementary material. It is clearly seen that the unmodified electrodes have almost the same increment (ΔR_{CT}) with a large standard deviation for both samples, suggesting that no specific antigen / antibody interaction is taking place. These results indicate that the use of unmodified steel mesh electrodes is not suitable for immunosensor application, being extremely necessary the steel mesh surface modification with PEDOT/AuNPs before the antigen immobilization, as proposed here.

It is important to describe here that the establishment of the cutoff value allows differentiating a serum sample as positive or negative for COVID-19 [81]. This set of measurements reflects the minimal expected R_{CT} signal for the serum additions to the electrolyte since the sample is a complex matrix containing other species that can interact with the electrode. Thus, the cutoff value can be determined by the mean plus three standard deviations (cutoff = mean + (3*SD)) [81, 88]. For now, we do not have enough sample quantity to determine reliable the

cutoff value, usually the works relate more than one hundred samples.

Conclusion

In summary, we developed a simple, selective, reliable and relatively fast-method to detect COVID-19 antibodies in real clinical serum samples. Raman and SEM-EDS results show that the electrode was successfully modified with PEDOT/AuNPs/AG/BSA, and SEM and TEM images confirm that the gold nanoparticles were uniformly distributed on PEDOT surface, allowing the antigen immobilization all over the electrode surface. The method applied here consists in analyzing the variation of the charge transference resistance of the electrode/electrolyte interface using $[Fe(CN)_6]^{3-/4-}$ as a probe; the differences in the R_{CT} values were observed due the specific antigen-antibody interaction. Also, for the dilution range studied here, it was obtained a minimum increase of 3.5-fold (% in ΔR_{CT} value) in positive serum samples than negative serum samples, suggesting the material has potential to be used as an impedimetric immunosensor to diagnose COVID-19 antibodies. However, in the future more clinical samples could be analyzed by this method in order to obtain the cutoff value and a quantitative test for antibodies could be studied to replace the traditional methods.

Declaration of Competing Interest

none.

The authors declare that they have no known competing financial interests or personal relationships that could have appeared to influence the work reported in this paper.

Acknowledgments

The authors would like to thank Brazilian agencies FAPERGS (Grant number: 20/2551-0000270-5) and CNPQ for funding and scholarship grants and IFFar. Also, the ISI-Eletroquímica-SENAI for the Raman facilities, Dr. Heloise Ribeiro de Barros for the TEM images realized at USP are kindly acknowledge. A.L.L and F.W also acknowledges Prof. Dr. Marcio Vidotti (GPMIn – UFPR) for the discussions and encouragement and for all technical support.

Supplementary materials

Supplementary material associated with this article can be found, in the online version, at doi:10.1016/j.electacta.2021.139757.

References

[1] Y. Orooji, H. Sohrabi, N. Hemmat, F. Oroojalian, B. Baradaran, A. Mokhtarzadeh, M. Mohaghegh, H. Karimi-Maleh, An overview on SARS-CoV-2 (COVID-19) and other human coronaviruses and their detection capability via amplification assay, Chem. Sens., Biosens., Immunosens. Clin. Assays, Nano-Micro Lett. 13 (2020) 18.

[2] H. Harapan, N. Itoh, A. Yufika, W. Winardi, S. Keam, H. Te, D. Megawati, Z. Hayati, A.L. Wagner, M. Mudatsir, Coronavirus disease 2019 (COVID-19): a literature review, J. Infect. Public Health 13 (2020) 667–673.

[3] World Health Organization, "Coronavirus disease (COVID-19), https://www.who.int/health-topics/coronavirus#tab=tab_1. September 2021.

[4] T. Hoffman, K. Nissen, J. Krambrich, B. Rönnberg, D. Akaberi, M. Esmaeilzadeh, E. Salaneck, J. Lindahl, Å. Lundkvist, Evaluation of a COVID-19 IgM and IgG rapid test; an efficient tool for assessment of past exposure to SARS-CoV-2, Infect. Ecol. Epidemiol. 10 (2020) 1754538.

[5] S.S. Mahshid, S.E. Flynn, S. Mahshid, The potential application of electrochemical biosensors in the COVID-19 pandemic: a perspective on the rapid diagnostics of SARS-CoV-2, Biosens. Bioelectron. 176 (2021) 112905.

[6] B. Mojsoska, S. Larsen, D.A. Olsen, J.S. Madsen, I. Brandslund, F.A.a. Alatraktchi, Rapid SARS-CoV-2 detection using electrochemical immunosensor, Sensors 21 (2021) 390.

[7] R. Antiochia, Nanobiosensors as new diagnostic tools for SARS, MERS and COVID-19: from past to perspectives, Microchim. Acta 187 (2020) 639.

[8] J.F. Hernández-Rodríguez, D. Rojas, A. Escarpa, Electrochemical sensing directions for next-generation healthcare: trends, challenges, and frontiers, Anal. Chem. 93 (2021) 167–183.

[9] Y. Wang, H. Xu, J. Zhang, G. Li, Electrochemical sensors for clinic analysis, Sensors 8 (2008) 2043–2081.

[10] D. Grieshaber, R. MacKenzie, J. Vörös, E. Reimhult, Electrochemical biosensors - sensor principles and architectures, Sensors, 8 (2008) 1400–1458.

[11] J. Monzó, I. Insua, F. Fernandez-Trillo, P. Rodriguez, Fundamentals, achievements and challenges in the electrochemical sensing of pathogens, Analyst 140 (2015) 7116–7128.

[12] D.R. Thévenot, K. Toth, R.A. Durst, G.S. Wilson, Electrochemical biosensors: recommended definitions and classification, Biosens. Bioelectron. 16 (2001) 121–131.

[13] M. Drobysh, A. Ramanaviciene, R. Viter, A. Ramanavicius, Affinity sensors for the diagnosis of COVID-19, Micromachines (Basel) 12 (2021) 390.

[14] M.T. Robert Săndulescu, Cecilia Cristea and Ede Bodoki materials for the construction of electrochemical biosensors, in: T. Rinken (Ed.), Biosensor Micro and Nanoscale applications, Ed., 2015, pp. 1–36.

[15] L.A. Layqah, S. Eissa, An electrochemical immunosensor for the corona virus associated with the Middle East respiratory syndrome using an array of gold nanoparticle-modified carbon electrodes, Microchim. Acta 186 (2019) 224.

[16] I. Plikusiene, V. Maciulis, A. Ramanaviciene, Z. Balevicius, E. Buzavaite-Verteliene, E. Ciplys, R. Slibinskas, M. Simanavicius, A. Zvirbliene, A. Ramanavicius, Evaluation of kinetics and thermodynamics of interaction between immobilized SARS-CoV-2 nucleoprotein and specific antibodies by total internal reflection ellipsometry, J. Colloid Interface Sci. 594 (2021) 195–203.

[17] C.d.C. Santos, P.C.M. Santos, K.L.S. Rocha, R.L. Thomasini, D.B. de Oliveira, D.L. Franco, L.F. Ferreira, A new tool for dengue virus diagnosis: optimization and detection of anti-NS1 antibodies in serum samples by impedimetric transducers, Microchem. J. 154 (2020) 104544.

[18] J. Cecchetto, F.C. Carvalho, A. Santos, F.C.B. Fernandes, P.R. Bueno, An impedimetric biosensor to test neat serum for dengue diagnosis, Sens. Actuat. B: Chem 213 (2015) 150–154.

[19] A. Kaushik, A. Yndart, S. Kumar, R.D. Jayant, A. Vashist, A.N. Brown, C.-.Z. Li, M. Nair, A sensitive electrochemical immunosensor for label-free detection of Zika-virus protein, Sci. Rep. 8 (2018) 9700.

[20] G. Cabral-Miranda, A.R. Cardoso, L.C.S. Ferreira, M.G.F. Sales, M.F. Bachmann, Biosensor-based selective detection of Zika virus specific antibodies in infected individuals, Biosens. Bioelectron. 113 (2018) 101–107.

[21] C. Akkapinyo, P. Khownarumit, D. Waraho-Zhmayev, R.P. Poo-Arporn, Development of a multiplex immunochromatographic strip test and ultrasensitive electrochemical immunosensor for hepatitis B virus screening, Anal. Chim. Acta 1095 (2020) 162–171.

[22] H. Alizadeh Zeinabad, H. Ghourchian, M. Falahati, M. Fathipour, M. Azizi, S.M. Boutorabi, Ultrasensitive interdigitated capacitance immunosensor using gold nanoparticles, Nanotechnology 29 (2018) 265102.

[23] J. Wan, J. Ai, Y. Zhang, X. Geng, Q. Gao, Z. Cheng, Signal-off impedimetric immunosensor for the detection of Escherichia coli O157:H7, Sci. Rep. 6 (2016) 19806.

[24] R. Jijie, K. Kahlouche, A. Barras, N. Yamakawa, J. Bouckaert, T. Gharbi, S. Szunerits, R. Boukherroub, Reduced graphene oxide/polyethylenimine based immunosensor for the selective and sensitive electrochemical detection of uropathogenic Escherichia coli, Sens. Actuat. B: Chem 260 (2018) 255–263.

[25] M.Z. Rashed, J.A. Kopechek, M.C. Priddy, K.T. Hamorsky, K.E. Palmer, N. Mittal, J. Valdez, J. Flynn, S.J. Williams, Rapid detection of SARS-CoV-2 antibodies using electrochemical impedance-based detector, Biosens. Bioelectron. 171 (2021) 112709.

[26] L. Fabiani, M. Saroglia, G. Galatà, R. De Santis, S. Fillo, V. Luca, G. Faggioni, N. D'Amore, E. Regalbuto, P. Salvatori, G. Terova, D. Moscone, F. Lista, F. Arduini, Magnetic beads combined with carbon black-based screen-printed electrodes for COVID-19: a reliable and miniaturized electrochemical immunosensor for SARS-CoV-2 detection in saliva, Biosens. Bioelectron. 171 (2021) 112686.

[27] S. Eissa, M. Zourob, Development of a low-cost cotton-tipped electrochemical immunosensor for the detection of SARS-CoV-2, Anal. Chem. 93 (2021) 1826–1833.

[28] R.M. Torrente-Rodríguez, H. Lukas, J. Tu, J. Min, Y. Yang, C. Xu, H.B. Rossiter, W. Gao, SARS-CoV-2 RapidPlex: a graphene-based multiplexed telemedicine platform for rapid and low-cost COVID-19 diagnosis and monitoring, Matter 3 (2020) 1981–1998.

[29] G.C. Zaccariotto, M.K.L. Silva, G.S. Rocha, I. Cesarino, A novel method for the detection of SARS-CoV-2 based on graphene-impedimetric immunosensor, Materials (Basel) 14 (2021).

[30] H. Beitollai, M. Safaei, S. Tajik, Application of Graphene and Graphene Oxide for modification of electrochemical sensors and biosensors: a review, Int. J. Nano Dimens. 10 (2019) 125–140.

[31] X.-.Q. Wu, J.-.G. Ma, H. Li, D.-.M. Chen, W. Gu, G.-.M. Yang, P. Cheng, Metal–organic framework biosensor with high stability and selectivity in a bio-mimic environment, Chem. Commun. 51 (2015) 9161–9164.

[32] V.V. Tran, N.H.T. Tran, H.S. Hwang, M. Chang, Development strategies of conducting polymer-based electrochemical biosensors for virus biomarkers: potential for rapid COVID-19 detection, Biosens. Bioelectron. 182 (2021) 113192.

[33] A. Majdalawieh, M.C. Kanan, O. El-Kadri, S.M. Kanan, Recent advances in gold and silver nanoparticles: synthesis and applications, J. Nanosci. Nanotechnol. 14 (2014) 4757–4780.

[34] S. Alireza Hashemi, S. Bahrani, S. Mojtaba Mousavi, N. Omidifar, N. Ghaleh Golab Behbahan, M. Arjmand, S. Ramakrishna, K. Bagheri Lankarani, M. Moghadami, M. Shokripour, M. Firoozsani, W.-.H. Chiang, Ultra-precise label-free nanosensor based on integrated graphene with Au nanostars toward direct detection of IgG antibodies of SARS-CoV-2 in blood, J. Electroanal. Chem. 894 (2021) 115341.
[35] H. Jans, Q. Huo, Gold nanoparticle-enabled biological and chemical detection and analysis, Chem. Soc. Rev. 41 (2012) 2849–2866.
[36] X. Wang, R. Niessner, D. Tang, D. Knopp, Nanoparticle-based immunosensors and immunoassays for aflatoxins, Anal. Chim. Acta 912 (2016) 10–23.
[37] S.A. Bansal, V. Kumar, J. Karimi, A.P. Singh, S. Kumar, Role of gold nanoparticles in advanced biomedical applications, Nanoscale Adv 2 (2020) 3764–3787.
[38] A. Sharma, A. Kumar, R. Khan, Electrochemical immunosensor based on poly (3,4-ethylenedioxythiophene) modified with gold nanoparticle to detect aflatoxin B(1), Mater. Sci. Eng. C Mater. Biol. Appl. 76 (2017) 802–809.
[39] S. Mandal, S. Phadtare, M. Sastry, Interfacing biology with nanoparticles, Curr. Appl Phys. 5 (2005) 118–127.
[40] B. Lakard, Electrochemical biosensors based on conducting polymers: a review, Appl. Sci. 10 (2020) 6614.
[41] M. Naseri, L. Fotouhi, A. Ehsani, Recent progress in the development of conducting polymer-based nanocomposites for electrochemical biosensors applications: a mini-review, Chem. Rec. 18 (2018) 599–618.
[42] S. Ramanavicius, A. Ramanavicius, Conducting polymers in the design of biosensors and biofuel cells, Polymers (Basel) 13 (2021) 49.
[43] A. Ramanavicius, Y. Oztekin, A. Ramanaviciene, Electrochemical formation of polypyrrole-based layer for immunosensor design, Sens. Actuat. B: Chem 197 (2014) 237–243.
[44] S. Shrivastava, N. Jadon, R. Jain, Next-generation polymer nanocomposite-based electrochemical sensors and biosensors: a review, TrAC - Trend Anal Chem 82 (2016) 55–67.
[45] A. Kukhta, A. Pochtenny, A. Misevich, I. Kukhta, E. Semenova, V. Svetlana, E. Sarantopoulou, Optical and electrophysical properties of nanocomposites based on PEDOT: PSS and gold/silver nanoparticles, Phys. Solid State 56 (2014) 827–834.
[46] D. Tonelli, E. Scavetta, I. Gualandi, Electrochemical deposition of nanomaterials for electrochemical sensing, Sensors 19 (2019) 1186.
[47] Y. Wen, J. Xu, Scientific importance of water-processable PEDOT–PSS and preparation, challenge and new application in sensors of its film electrode: a review, J. Polym. Sci. A Polym. Chem. 55 (2017) 1121–1150.
[48] Y. Hui, C. Bian, S. Xia, J. Tong, J. Wang, Synthesis and electrochemical sensing application of poly(3,4-ethylenedioxythiophene)-based materials: a review, Anal. Chim. Acta 1022 (2018) 1–19.
[49] N. Pogulyaichenko, S. Hui, V. Malev, V. Kondratiev, Gold electroless deposition into poly-3,4-ethylenedioxythiophene films, Russ. J. Electrochem. 45 (2009) 1176–1182.
[50] E.B. Bahadır, M.K. Sezgintürk, A review on impedimetric biosensors, Artif. Cells Nanomed. Biotechnol. 44 (2016) 248–262.
[51] Z.-.D. Guo, Z.-.Y. Wang, S.-.F. Zhang, X. Li, L. Li, C. Li, Y. Cui, R.-.B. Fu, Y.-.Z. Dong, X.-.Y. Chi, M.-.Y. Zhang, K. Liu, C. Cao, B. Liu, K. Zhang, Y.-.W. Gao, B. Lu, W. Chen, Aerosol and surface distribution of severe acute respiratory syndrome coronavirus 2 in hospital wards, Wuhan, China, 2020, Emerg. Infect. Dis. 26 (2020) 1583–1591.
[52] T.R. Tozetto-Mendoza, K.A. Kanunfre, L.S. Vilas-Boas, E.P. Sanchez Espinoza, H.G.O. Paião, M.C. Rocha, A.V. de Paula, M.S. de Oliveira, D.B. Zampelli, J.M. Vieira, L. Buss, S.F. Costa, E.C. Sabino, S.S. Witkin, T.S. Okay, M.C. Mendes–Correa, Nucleoprotein-based ELISA for detection of SARS-COV-2 IgG antibodies: could an old assay be suitable for serodiagnosis of the new coronavirus? J. Virol. Methods 290 (2021) 114064.
[53] P. Krishnaveni, V. Ganesh, Electron transfer studies of a conventional redox probe in human sweat and saliva bio-mimicking conditions, Sci. Rep. 11 (2021) 7663.
[54] M. Sterby, R. Emanuelsson, X. Huang, A. Gogoll, M. Strømme, M. Sjödin, Characterization of PEDOT-quinone conducting redox polymers for water based secondary batteries, Electrochim. Acta 235 (2017) 356–364.
[55] S. Moulton, J.N. Barisci, A. Bath, R. Stella, G. Wallace, Investigation of protein adsorption and electrochemical behavior at a gold electrode, J. Colloid Interface Sci. 261 (2003) 312–319.
[56] I. Willner, S. Rubin, Y. Cohen, Photoregulated binding of spiropyran-modified concanavalin A to monosaccharide-functionalized self-assembled monolayers on gold electrodes, J. Am. Chem. Soc. 115 (1993) 4937–4938.
[57] A. Medhi, S. Baruah, J. Singh, C.A. Betty, D. Mohanta, Au nanoparticle modified GO/PEDOT-PSS based immunosensor probes for sensitive and selective detection of serum immunoglobulin g (IgG), Appl. Surf. Sci. 575 (2022) 151775.
[58] Z. Wang, A. Murphy, A. O'Riordan, I. O'Connell, Equivalent impedance models for electrochemical nanosensor-based integrated system design, Sensors 21 (2021) 3259.
[59] L.F.Q.P. Marchesi, F.R. Simões, L.A. Pocrifka, E.C. Pereira, Investigation of polypyrrole degradation using electrochemical impedance spectroscopy, J. Phys. Chem. B 115 (2011) 9570–9575.
[60] A. Ramanavicius, A. Finkelsteinas, H. Cesiulis, A. Ramanaviciene, Electrochemical impedance spectroscopy of polypyrrole based electrochemical immunosensor, Bioelectrochemistry 79 (2010) 11–16.
[61] J. Mostany, B.R. Scharifker, Impedance spectroscopy of undoped, doped and overoxidized polypyrrole films, Synthetic Met 87 (1997) 179–185.
[62] F. Wolfart, B.M. Hryniewicz, M.S. Góes, C.M. Corrêa, R. Torresi, M.A.O.S. Minadeo, S.I. Córdoba de Torresi, R.D. Oliveira, L.F. Marchesi, M. Vidotti, Conducting polymers revisited: applications in energy, electrochromism and molecular recognition, J. Solid State Electrochem. 21 (2017) 2489–2515.
[63] C. Fernández-Sánchez, C.J. McNeil, K. Rawson, Electrochemical impedance spectroscopy studies of polymer degradation: application to biosensor development, Trends Anal. Chem. 24 (2005) 37–48.
[64] F. Wolfart, B.M. Hryniewicz, L.F. Marchesi, E.S. Orth, D.P. Dubal, P. Gómez-Romero, M. Vidotti, Direct electrodeposition of imidazole modified poly(pyrrole) copolymers: synthesis, characterization and supercapacitive properties, Electrochim. Acta 243 (2017) 260–269.
[65] J. Sopoušek, J. Věžník, J. Houser, P. Skládal, K. Lacina, Crucial factors governing the electrochemical impedance on protein-modified surfaces, Electrochim. Acta 388 (2021) 138616.
[66] S. Omanovic, S.G. Roscoe, Interfacial behavior of beta-lactoglobulin at a stainless steel surface: an electrochemical impedance spectroscopy study, J. Colloid Interface Sci. 227 (2000) 452–460.
[67] A.L. Soares, M.L. Zamora, L.F. Marchesi, M. Vidotti, Adsorption of catechol onto PEDOT films doped with gold nanoparticles: electrochemical and spectroscopic studies, Electrochim. Acta 322 (2019) 134773.
[68] I. Rocha, E. Lucht, I.C. Riegel-Vidotti, M. Vidotti, E.S. Orth, Kinetic approach to elucidate size controllable features in nanocomposites of gold nanoparticles and poly(3,4-ethylenedioxythiophene) in aqueous dispersion stabilized by gum acacia, J. Phys. Chem. C 118 (2014) 25756–25764.
[69] S. Radhakrishnan, C. Sumathi, V. Dharuman, J. Wilson, Gold nanoparticles functionalized poly(3,4-ethylenedioxythiophene) thin film for highly sensitive label free DNA detection, Anal. Methods 5 (2013) 684–689.
[70] W. Shi, Q. Yao, S. Qu, H. Chen, T. Zhang, L. Chen, Micron-thick highly conductive PEDOT films synthesized via self-inhibited polymerization: roles of anions, NPG Asia Mater 9 (2017) e405-e405.
[71] A.C.d. Silva, A.O.S. Marco, Gold Nanoparticles and [PEDOT-Poly(D,L-Lactic Acid)] Composite: synthesis, Characterization and Application to H2O2 Sensing, J. Braz. Chem. Soc. 30 (2019) 2066–2075.
[72] W.W. Chiu, J. Travaš-Sejdić, R.P. Cooney, G.A. Bowmaker, Studies of dopant effects in poly(3,4-ethylenedi-oxythiophene) using Raman spectroscopy, J. Raman Spectrosc. 37 (2006) 1354–1361.
[73] S. Garreau, G. Louarn, J.P. Buisson, G. Froyer, S. Lefrant, In situ spectroelectrochemical raman studies of poly(3,4-ethylenedioxythiophene) (PEDT), Macromolecules 32 (1999) 6807–6812.
[74] E. Pensa, E. Cortés, G. Corthey, P. Carro, C. Vericat, M.H. Fonticelli, G. Benítez, A.A. Rubert, R.C. Salvarezza, The chemistry of the sulfur–gold interface: in search of a unified model, Acc. Chem. Res. 45 (2012) 1183–1192.
[75] B.R. Moraes, N.S. Campos, C.M.S. Izumi, Surface-enhanced Raman scattering of EDOT and PEDOT on silver and gold nanoparticles, Vib. Spectrosc. 96 (2018) 137–142.
[76] R.P. Kengne-Momo, P. Daniel, F. Lagarde, Y.L. Jeyachandran, J.F. Pilard, M.J. Durand-Thouand, G. Thouand, Protein interactions investigated by the Raman spectroscopy for biosensor applications, Int. J. Spectrosc. 2012 (2012) 462901.
[77] N. Kuhar, S. Sil, T. Verma, S. Umapathy, Challenges in application of Raman spectroscopy to biology and materials, RSC Adv. 8 (2018) 25888–25908.
[78] S. Patra, K. Barai, N. Munichandraiah, Scanning electron microscopy studies of PEDOT prepared by various electrochemical routes, Synth. Met. 158 (2008) 430–435.
[79] U. Lang, E. Müller, N. Naujoks, J. Dual, Microscopical investigations of PEDOT:PSS thin films, Adv. Funct. Mater. 19 (2009) 1215–1220.
[80] P. Pavani, K. Kumar, A. Rani, P. Venkatesu, M.-.J. Lee, The influence of sodium phosphate buffer on the stability of various proteins: insights into protein-buffer interactions, J. Mol. Liq. 331 (2021) 115753.
[81] O. Parkash, M.A. Abdullah, C.Y. Yean, S.D. Sekaran, R.H. Shueb, Development and evaluation of an electrochemical biosensor for detection of dengue-specific IGM antibody in serum samples, Diagnostics 11 (2021) 33.
[82] S. Campuzano, F. Kuralay, M.J. Lobo-Castañón, M. Bartošík, K. Vyavahare, E. Paleček, D.A. Haake, J. Wang, Ternary monolayers as DNA recognition interfaces for direct and sensitive electrochemical detection in untreated clinical samples, Biosens. Bioelectron. 26 (2011) 3577–3583.
[83] J.Y. Lichtenberg, Y. Ling, S. Kim, Non-specific adsorption reduction methods in biosensing, Sensors (Basel) 19 (2019) 2488.
[84] T.A.R. Cordeiro, M.V.C. Gonçalves, D.L. Franco, A.B. Reis, H.R. Martins, L.F. Ferreira, Label-free electrochemical impedance immunosensor based on modified screen-printed gold electrodes for the diagnosis of canine visceral leishmaniasis, Talanta 195 (2019) 327–332.
[85] B.V.M. Silva, M.T. Cordeiro, M.A.B. Rodrigues, E.T.A. Marques, R.F. Dutra, A label and probe-free Zika virus immunosensor prussian blue@carbon nanotube-based for amperometric detection of the NS2B protein, Biosensors 11 (2021) 157.
[86] N.C. Cady, N. Tokranova, A. Minor, N. Nikvand, K. Strle, W.T. Lee, W. Page, E. Guignon, A. Pilar, G.N. Gibson, Multiplexed detection and quantification of human antibody response to COVID-19 infection using a plasmon enhanced biosensor platform, Biosens. Bioelectron. 171 (2021) 112679.
[87] J.D. Whitman, J. Hiatt, C.T. Mowery, B.R. Shy, R. Yu, T.N. Yamamoto, U. Rathore, G.M. Goldgof, C. Whitty, J.M. Woo, A.E. Gallman, T.E. Miller, A.G. Levine, D.N. Nguyen, S.P. Bapat, J. Balcerek, S.A. Bylsma, A.M. Lyons, S. Li, A.W.-y. Wong, E.M. Gillis-Buck, Z.B. Steinhart, Y. Lee, R. Apathy, M.J. Lipke, J.A. Smith, T. Zheng, I.C. Boothby, E. Isaza, J. Chan, D.D. Acenas, J. Lee, T.A. Macrae, T.S. Kyaw, D. Wu, D.L. Ng, W. Gu, V.A. York, H.A. Eskandarian, P.C. Callaway, L. Warrier, M.E. Moreno, J. Levan, L. Torres, L.A. Far-

rington, R.P. Loudermilk, K. Koshal, K.C. Zorn, W.F. Garcia-Beltran, D. Yang, M.G. Astudillo, B.E. Bernstein, J.A. Gelfand, E.T. Ryan, R.C. Charles, A.J. Iafrate, J.K. Lennerz, S. Miller, C.Y. Chiu, S.L. Stramer, M.R. Wilson, A. Manglik, C.J. Ye, N.J. Krogan, M.S. Anderson, J.G. Cyster, J.D. Ernst, A.H.B. Wu, K.L. Lynch, C. Bern, P.D. Hsu, A. Marson, Evaluation of SARS-CoV-2 serology assays reveals a range of test performance, Nat. Biotechnol. 38 (2020) 1174–1183.

[88] S.K. Elledge, X.X. Zhou, J.R. Byrnes, A.J. Martinko, I. Lui, K. Pance, S.A. Lim, J.E. Glasgow, A.A. Glasgow, K. Turcios, N.S. Iyer, L. Torres, M.J. Peluso, T.J. Henrich, T.T. Wang, C.M. Tato, K.K. Leung, B. Greenhouse, J.A. Wells, Engineering luminescent biosensors for point-of-care SARS-CoV-2 antibody detection, Nat. Biotechnol. 39 (2021) 928–935.